

Accepted Manuscript

Loading AgCl@Ag on phosphotungstic acid modified macrocyclic coordination compound: Z-scheme photocatalyst for persistent pollutant degradation and hydrogen evolution

Shunqiang Chen, Feng Li, Taohai Li, Wei Cao

PII: S0021-9797(19)30390-X
DOI: <https://doi.org/10.1016/j.jcis.2019.03.092>
Reference: YJCIS 24813

To appear in: *Journal of Colloid and Interface Science*

Received Date: 21 January 2019
Revised Date: 26 March 2019
Accepted Date: 28 March 2019

Please cite this article as: S. Chen, F. Li, T. Li, W. Cao, Loading AgCl@Ag on phosphotungstic acid modified macrocyclic coordination compound: Z-scheme photocatalyst for persistent pollutant degradation and hydrogen evolution, *Journal of Colloid and Interface Science* (2019), doi: <https://doi.org/10.1016/j.jcis.2019.03.092>

This is a PDF file of an unedited manuscript that has been accepted for publication. As a service to our customers we are providing this early version of the manuscript. The manuscript will undergo copyediting, typesetting, and review of the resulting proof before it is published in its final form. Please note that during the production process errors may be discovered which could affect the content, and all legal disclaimers that apply to the journal pertain.



**Loading AgCl@Ag on phosphotungstic acid modified macrocyclic
coordination compound: Z-scheme photocatalyst for persistent
pollutant degradation and hydrogen evolution**

Shunqiang Chen^a, Feng Li^a, Taohai Li^{a*} and Wei Cao^b

^a*College of Chemistry, Key Lab of Environment Friendly Chemistry and Application
in Ministry of Education, Xiangtan University, Xiangtan, 411105, China.*

^b*Nano and Molecular Materials Research Unit, Faculty of Science, University of
Oulu, P.O. Box 3000, FIN-90014, Finland*

* Correspondence Author. Tel.: +86-731-58292202; fax: +86-731-8292251;

E-mail address: hnlth@xtu.edu.cn(T. Li).

Abstract

In this work, Z-scheme photocatalysts of $(\text{CuC}_{10}\text{H}_{26}\text{N}_6)_3(\text{PW}_{12}\text{O}_{40})_2 / \text{AgCl}@\text{Ag}$ were designed and realized for effective removal of solvable and insoluble persistent organic pollutants and hydrogen evolution under simulated sunlight. The catalysts were synthesized via a simple hydrothermal-chemical co-precipitation method. Excellent photocatalytic abilities are demonstrated in degradations of persistent pollutant 2, 4-Dinitrophenol (DNP) and tetracycline (TC) under simulated sunlight, as well as a high H_2 production rate of $19.28 \mu\text{mol g}^{-1} \text{h}^{-1}$. Through structural, morphological, radical, and electrochemical determinations, the photocatalytic mechanism was studied, and attributed to effective separations of charge carriers between the heterojunctional counterparts of $(\text{CuC}_{10}\text{H}_{26}\text{N}_6)_3(\text{PW}_{12}\text{O}_{40})_2$ and $\text{AgCl}@\text{Ag}$.

Keywords: Z-scheme; Polyoxometalate; $\text{AgCl}@\text{Ag}$; Photocatalyst; Pollutant

1. Introduction

As typical photocatalysts for energy production and water treatment,¹ semiconductor heterojunctions are generally categorized into two dominant types of conventional and Z-scheme heterojunctions. The former ones, though widely developed, suffer from two shortcomings: (i) The redox abilities of photogenerated electrons and holes are remarkably weakened after charge migrations. (ii) Electron transfers between the joint counterparts are difficult due to strong Coulomb repulsions.^{2,3} On the contrary, the direct Z-scheme mechanism can retain strong reductive and oxidative abilities, and further inhibit electron-hole pair recombinations.⁴ Among various materials involved in the Z-scheme structures, the AgCl is a promising modifier thanks to its nontoxicity and easy preparation.^{5,6} For instance, the hierarchical Ag@AgCl/BiVO₄ catalyst was reportedly owning enhanced photocatalytic activities than the pure BiVO₄.⁷ The Z-scheme AgCl/Ag/CaTiO₃ nanomaterials were synthesized and found useful for photocatalytic hydrogen production.⁸ Despite these successes, degradations of solid organic pollutants are still out of the Z-scheme chemicals' reach. In addition to chemical stabilities of these contaminants, the low-band-gap joining partner can neither offer enough energies to oxidize organics, nor delay electron-hole recombinations to accomplish decomposing processes. Therefore, new Z-scheme photocatalytic systems with proper bandgaps are desired for general photocatalytic applications.

The polyoxometalates (POMs) may act as good joining counterparts to the AgCl in Z-scheme catalyst designs. Constituted by the W, Mo, V, Nb, or Ta ions in high oxidation states,⁹⁻¹³ the anionic metal-oxo clusters have already shown remarkable redox abilities and wide applications in catalysis.^{14,15} The POMs, especially the Keggin-type heteropolytungstates ($\text{PW}_{12}\text{O}_{40}^{3-}$, $\text{SiW}_{12}\text{O}_{40}^{4-}$, $\text{BW}_{12}\text{O}_{40}^{5-}$, $\text{FeW}_{12}\text{O}_{40}^{5-}$ and $\text{H}_2\text{W}_{12}\text{O}_{40}$), own unique H_2 evolution abilities in acidic solutions under UV-light radiation along with their decontamination perspectives.¹⁶⁻²⁰ However, hydrogen emission from the acidic ambiances is not resulted from the photocatalytic hydrogen evolution (PHE) process during which creation of protons should be subjected photoeffects. Indeed, the Keggin-type heteropolytungstages are not capable for PHE and photocatalytic degradation. The POMs are easily dissolved in aqueous ambiances, and unsuitable in water reduction due to their low reduction potential. In addition, their intrinsic electronic structures are not suitable for visible-light absorptions. However, it is noticed that combining proper coordination compound with the POMs can prevent dissolution during proton reduction processes.²¹ Based on these evidences, a new type of Z-scheme heterojunctions may be formed from the AgCl and macrocyclic coordination compounds (MCCs) loaded POMs for solid pollutant decontamination and PHE under simulated sunlight.

In this work, we designed and prepared the $(\text{CuC}_{10}\text{H}_{26}\text{N}_6)_3(\text{PW}_{12}\text{O}_{40})_2$ /AgCl@Ag composites to reach a Z-scheme photocatalytic system. Synthesis was performed through a simple hydrothermal-chemical co-precipitation method. The

$(\text{CuC}_{12}\text{H}_{30}\text{N}_6)^{2+}$ ions of the MCC were bonded with the $\text{PW}_{12}\text{O}_{40}$ parts to tune overall bandgap energy and enable visible light absorption. The Z-scheme catalysts are empowered with strong redox abilities and right to inhibit recombinations of photogenerated charges. As a result, enhanced visible-light driven photoactivities are provided for solid pollutant degradation and H_2 evolution. Assessed from electrochemical characterizations, the photocatalytic mechanism of the Z-scheme structure was also revealed. In addition to successes in materials development, this work is hoped to initiate a new route of Z-scheme photocatalyst design by using the macrocyclic coordination compound modified POMs as joining candidates to other wide bandgap semiconductors.

2. Experimental

2.1 Materials and general synthetic strategy

The synthesis was performed in 2 steps. First, the $\text{CuC}_{10}\text{H}_{26}\text{N}_6\text{Cl}_2\text{O}_8$ MCC was prepared to modify the $\text{H}_3\text{PW}_{12}\text{O}_{40}$ (phosphotungstic acid) POM, yielding the MCC-POM reagent as a part in the Z-scheme photocatalysts. Later, the Ag (argentum) buffer was formed between the MCC-POM and the AgCl (silver chloride) counterparts in a co-precipitation procedure.

2.2 Synthesis of $(\text{CuC}_{10}\text{H}_{26}\text{N}_6)_3(\text{PW}_{12}\text{O}_{40})_2$

Synthesis of $\text{CuC}_{10}\text{H}_{26}\text{N}_6\text{Cl}_2\text{O}_8$: $\text{CuCl}_2 \cdot 2\text{H}_2\text{O}$ (copper(II) chloride dihydrate, 8.5 g) was added to a solution mixture of methanol (50 mL), $\text{C}_2\text{H}_8\text{N}_2$ (ethylenediamine, 6.80 mL), CH_2O (formaldehyde, 20.00 mL), and CH_3NH_2 (methylamine, 8.60 mL). After the $\text{CuCl}_2 \cdot 2\text{H}_2\text{O}$ was dissolved, the solution was heated and stirred under reflux for 24 hours. Excessive perchloric acid was added to the solution. The purple red crystals were removed, washed and recrystallized.

Synthesis of $(\text{CuC}_{10}\text{H}_{26}\text{N}_6)_3(\text{PW}_{12}\text{O}_{40})_2$: In a typical procedure, 0.78g $\text{CuC}_{10}\text{H}_{26}\text{N}_6\text{Cl}_2\text{O}_8$ and 2.88 g $\text{H}_3\text{PW}_{12}\text{O}_{40}$ were dissolved in 30ml distilled water by stirring at 50°C for 1h. After that, the pink $(\text{CuC}_{10}\text{H}_{26}\text{N}_6)_3(\text{PW}_{12}\text{O}_{40})_2$ precipitate was collected in vacuum filtration and washed three times by water and ethanol, and then vacuum dried at 60°C for 12 h.

2.3 Preparation of $(\text{CuC}_{10}\text{H}_{26}\text{N}_6)_3(\text{PW}_{12}\text{O}_{40})_2/\text{AgCl}@ \text{Ag}$

$(\text{CuC}_{10}\text{H}_{26}\text{N}_6)_3(\text{PW}_{12}\text{O}_{40})_2/\text{AgCl}@ \text{Ag}$ photocatalysts were prepared by a facile *in situ* co-precipitation method. In brief, 1.00 g $(\text{CuC}_{10}\text{H}_{26}\text{N}_6)_3(\text{PW}_{12}\text{O}_{40})_2$ was dispersed in distilled water (20.00 mL) and stirred 30 min to get a uniform solution (named as Solution A). Moreover, AgNO_3 (silver nitrate, 10mL, 0.10M) was added to Solution A. Afterwards, NaCl solution (sodium chloride, 0.10 M, 20.00 mL) was slowly dripped into the solution which was later stirred for 1 h in dark. The suspension solution was then irradiated for 30 min under a 500W Xe lamp. Powders were washed

several times with distilled water and ethanol. The $(\text{CuC}_{10}\text{H}_{26}\text{N}_6)_3(\text{PW}_{12}\text{O}_{40})_2/\text{AgCl@Ag}$ (CPA) composite with the Ag mass ratios of 9.75 wt% was obtained after being dried in a vacuum oven at 60°C for 24 h. Following the same protocol, the CPA composites with different Ag mass ratios can be synthesized by varying the AgNO_3 quantity. In total, five CPA composites were prepared with the Ag weight ratios of 0.00, 5.12, 9.75, 13.94 and 17.76 wt%. They are named as CPA-0, CPA-1, CPA-2, CPA-3 and CPA-4.

2.4 Characterizations

The as-prepared sample microstructures were analysed by x-ray diffraction (XRD). Morphological determinations were performed on a JSM-6610LV Scanning Electron Microscope (SEM) and a FEI Tecnai G20 transmission electron microscope (TEM). A Perkin-Elmer PHI 5000C spectrometer was employed to record X-ray photoelectron spectra (XPS) using a monochromatized Al $K\alpha$ excitation as the incident source, and adventurous carbon 1s binding energy (284.6 eV) for energy calibration. The Fourier-transform infrared spectroscopy (FTIR) was employed to analyze functional groups of samples. Measurements were carried on a Nicolet 6770 FTIR Spectrometric. The UV-vis diffuse reflectance spectra were obtained using a UV-vis spectrophotometer (UV-2550, Japan). Samples were dry-pressed to thin films during the tests.

2.5 Photoluminescence, electrochemical measurements, and electron spin resonance

To fully explore the photocatalytic mechanism, the photoluminescence (PL), electron spin resonance (ESR), and electrochemical determinations were carried out. The PL spectra were measured on an LS55 fluorescence spectrometer with an incident light source of 485 nm wavelength. The ESR signals were collected from radicals spin-trapped by the spin-trapping reagent 5, 5-dimethyl-1-pyrroline N-oxide (DMPO) on a Bruker A300 spectrometer. In the electrochemical tests, sample were dripped onto a $1 \times 1 \text{ cm}^2$ F-doped tin oxide (FTO) electrode. All electrochemical tests were performed on an electrochemical workstation (CHI650D, CH Instruments Inc. Shanghai). It is a typical three-electrode setup with an electrolyte solution of 0.5 M Na_2SO_4 .

2.6 Photocatalytic measurements

The photocatalytic performance of as-prepared catalysts was evaluated by decompositions of 2, 4-Dinitrophenol (DNP, 10mg/L), tetracycline (TC, 20 mg /L), and removal of the model dyes of rhodamine B (RhB, 10 mg/ L) and aqueous Cr (VI) ions in water (10 mg/L). Typically, 100 mg of as-prepared sample was added into 100mL of aqueous solution with target pollutants. Then, adsorption was carried out in the dark for 30 minutes to reach adsorption equilibrium. After simulated sunlight illumination (500 W Xe arc lamp), 3 mL aqueous solution was taken out at pre-set

time intervals and separated by centrifugation. The concentration of target pollutants left in the supernatant solution was determined by using UV carry-60–vis.

The photocatalytic hydrogen evolution experiments employed the as-prepared samples as the photocatalysts and gas circulation system for gas collection. In each experiment, 25 mg of photocatalyst was added to 50 mL of aqueous solution, which comprised 10 vol % triethanolamine (TEOA) as the sacrificial reagent. A 300 W Xe arc lamp was used as light source, and a gas chromatograph (GC-6890A) for hydrogen quantification.

3. Results and discussion

Figure 1 shows XRD patterns of the as-prepared CPA composites. Diffraction peaks of CPA-n (n=1-4) match well with those from CPA-0. Notably, no shift was found in the peak positions of $(\text{CuC}_{10}\text{H}_{26}\text{N}_6)_3(\text{PW}_{12}\text{O}_{40})_2$. This demonstrates that the load of AgCl@Ag on $(\text{CuC}_{10}\text{H}_{26}\text{N}_6)_3(\text{PW}_{12}\text{O}_{40})_2$ does not distort crystal structure of the MCC-POM frames. Increase of the AgCl@Ag content leads to emerging and increase of new diffraction peaks. Peaks of $2\theta=27.83^\circ$, 32.24° , 46.23° , 54.83° , 57.48° , 67.47° and 76.73° are indexed to the AgCl (111), (200), (220), (311), (222), (400) and (420) planes, respectively (JCPDS No:31-1238). The diffraction peak at 38.12° was attributed to (111) crystal phases of metallic Ag (JCPDS No: 87-717).²²

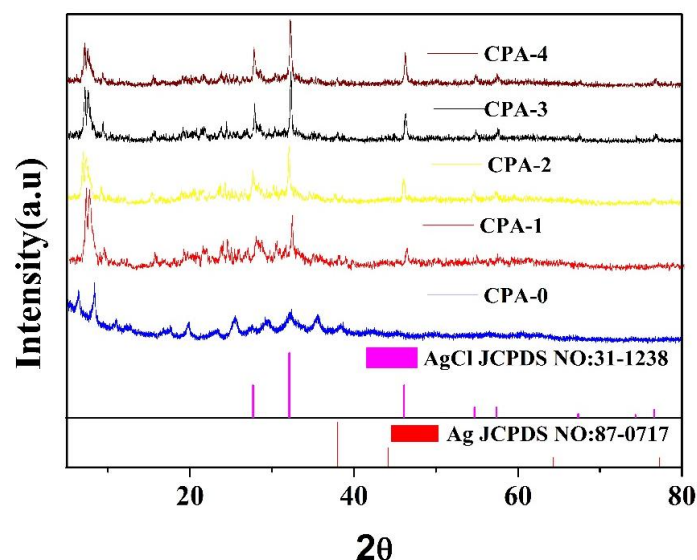


Figure 1. The XRD spectra of the $(\text{CuC}_{10}\text{H}_{26}\text{N}_6)_3(\text{PW}_{12}\text{O}_{40})_2$ loaded with different ratio of AgCl@Ag.

The microstructures of the $(\text{CuC}_{10}\text{H}_{26}\text{N}_6)_3(\text{PW}_{12}\text{O}_{40})_2/\text{AgCl@Ag}$ composites were further investigated by FTIR spectroscopy (Figure 2). The absorption peaks at 3237 and 1619 cm^{-1} were attributed to $\nu_{\text{N-H}}$ and $\nu_{\text{C=C}}$ stretching vibrations, while 1464 and 1288 cm^{-1} bands to methyl. The PW_{12} group owns four characteristics bands at 1082 (P-O_a), 977 (W=O_d), 896 ($\text{W-O}_b\text{-W}$), and 815 ($\text{W-O}_c\text{-W}$) cm^{-1} . This proves successful preparations of the $(\text{CuC}_{10}\text{H}_{26}\text{N}_6)_3(\text{PW}_{12}\text{O}_{40})_2$. The AgCl@Ag attachment to the $(\text{CuC}_{10}\text{H}_{26}\text{N}_6)_3(\text{PW}_{12}\text{O}_{40})_2$ did not destroy the microstructures of the foreign nanoparticles or the matrix, in line with the XRD results. No impurity peaks are found in Figure 2.

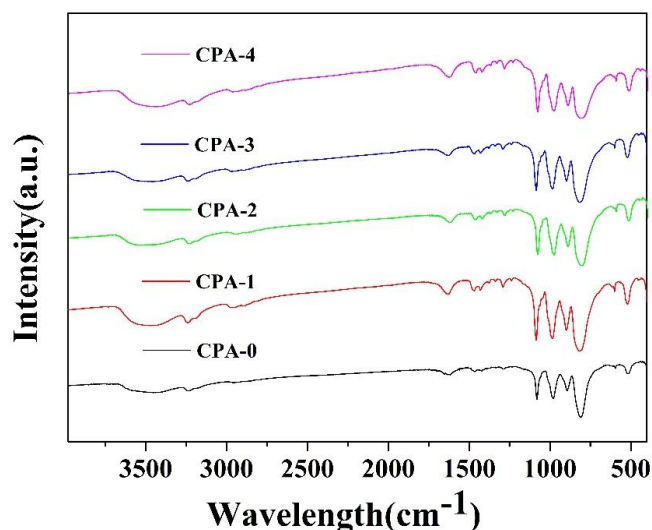


Figure 2. FTIR spectra of $(\text{CuC}_{10}\text{H}_{26}\text{N}_6)_3(\text{PW}_{12}\text{O}_{40})_2$ loaded with different ratio of AgCl@Ag.

Figure 3 depicts morphologies of $(\text{CuC}_{10}\text{H}_{26}\text{N}_6)_3(\text{PW}_{12}\text{O}_{40})_2$ loaded without and with the AgCl@Ag composite. As shown in Figure 3a, the $(\text{CuC}_{10}\text{H}_{26}\text{N}_6)_3(\text{PW}_{12}\text{O}_{40})_2$ are in the form of 3 dimensional flakes. These thin and irregular matrices can provide sufficient specific surface areas and sites to anchor noble metals.²³ Figures 3b-f are the SEM images of the CPA-1, CPA-2, CPA-3 and CPA-4. In Figure 3b, the AgCl@Ag nanoparticles turn out as tiny nano-nodules on the surfaces of $(\text{CuC}_{10}\text{H}_{26}\text{N}_6)_3(\text{PW}_{12}\text{O}_{40})_2$ flakes. Moreover, surface roughness increases with the amount of the AgCl@Ag additive. To clarify element distribution, the energy dispersive spectral (EDS) map was taken for CPA-2 and shown in Figure S1. Clear C, O, Cu, P, W, Ag and Cl elements locate uniformly in the selected area. The SEM results suggested that AgCl@Ag is successfully attached to the $(\text{CuC}_{10}\text{H}_{26}\text{N}_6)_3(\text{PW}_{12}\text{O}_{40})_2$ matrix.

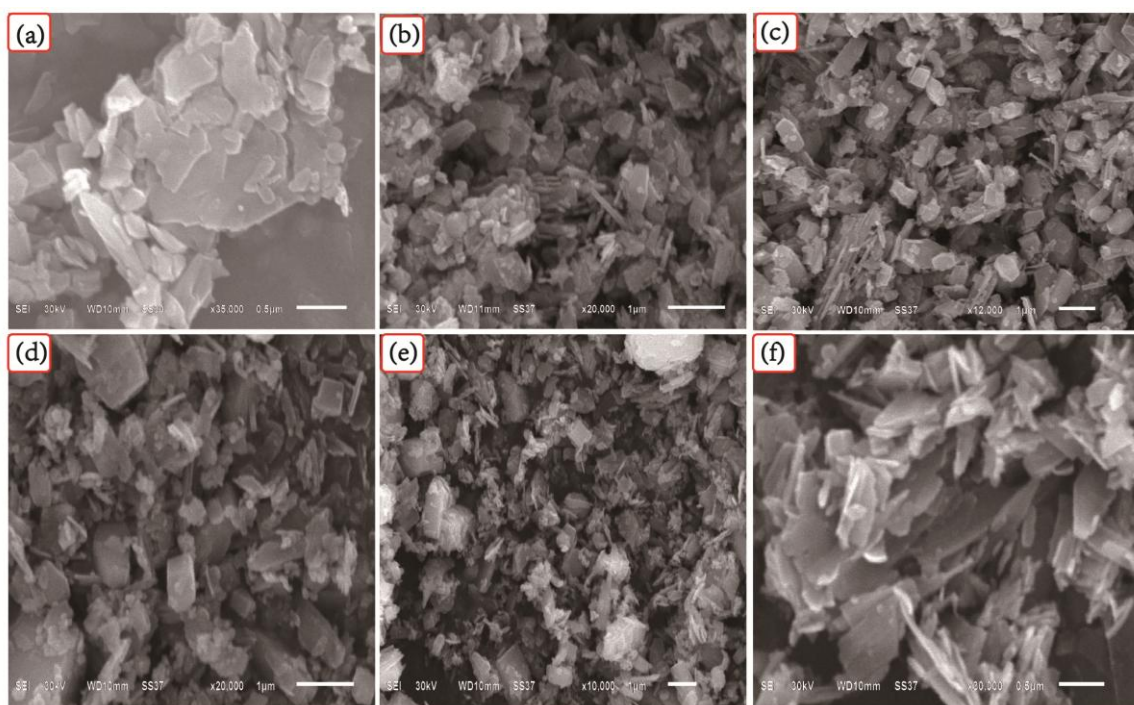


Figure 3. The SEM of the as-prepared samples with different ratio, (a) CPA-0, (b) CPA-1, (c) CPA-2, (d) CPA-3, (e) CPA-4 and (f) CPA-2.

The TEM and HRTEM determinations were performed for CPA-2 composite and visualized in Figure 4. Many AgCl@Ag nanoparticles are visible on the thin $(\text{CuC}_{10}\text{H}_{26}\text{N}_6)_3(\text{PW}_{12}\text{O}_{40})_2$ flakes. The AgCl@Ag nanoparticles connect tightly to surface and edge of $(\text{CuC}_{10}\text{H}_{26}\text{N}_6)_3(\text{PW}_{12}\text{O}_{40})_2$ in Figures 4a-c. The $(\text{CuC}_{10}\text{H}_{26}\text{N}_6)_3(\text{PW}_{12}\text{O}_{40})_2$ and AgCl@Ag can offer migration tunnels for the photogenerated carriers and improve photocatalytic performance.²³ In Figure 4d, the lattice spacing of 0.167 nm and 0.321 nm can be indexed to the (3 3 1) and (1 1 1) planes of AgCl. The lattice spacing of 0.205 nm and 0.1442 nm correlate to the (2 0 0) and (2 2 0) planes of Ag^0 . The AgCl@Ag nanoparticles have been connected to $(\text{CuC}_{10}\text{H}_{26}\text{N}_6)_3(\text{PW}_{12}\text{O}_{40})_2$ flakes successfully. The Z-scheme interface is further

explicated in Figure 4e, as shown by CuPW flakes and AgCl@Ag nanoparticles. The EDS map (Figure 4f) proves the overlap of Ag, Cl, Cu, and W.

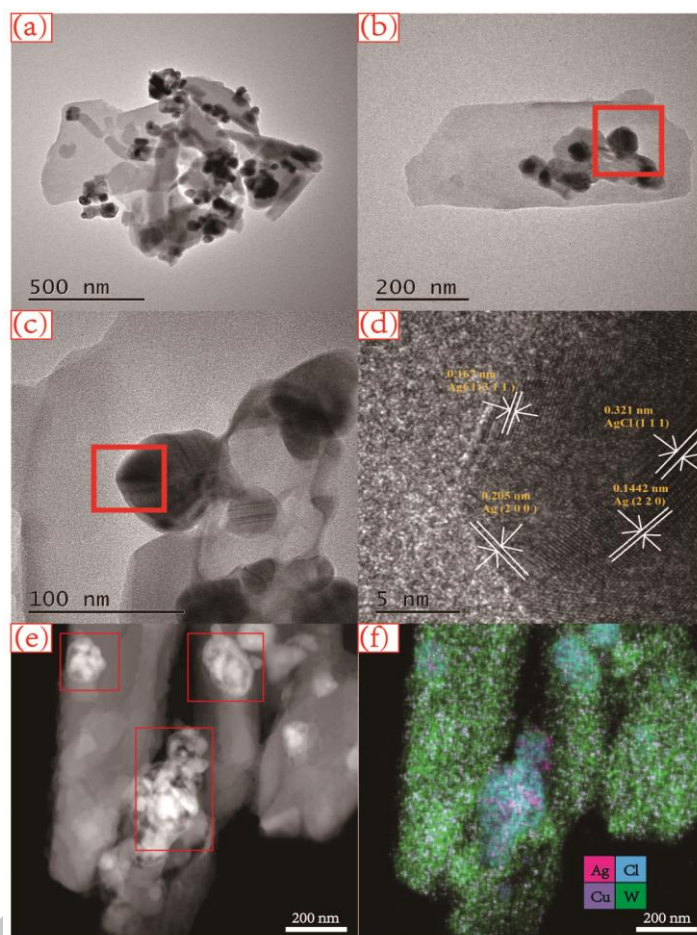


Figure 4. (a-c) TEM image of CPA-2, (d) HETEM image of CPA-2, (e) Dark field TEM images of CPA-2, (f) TEM-EDS mapping of CPA-2.

Chemical states of elements in the CPA-2 composite were further investigated. The Cu, C, N, Ag and Cl are identified in a general XPS survey in Figure 5a, indicating the coexistence of $(\text{CuC}_{10}\text{H}_{26}\text{N}_6)_3(\text{PW}_{12}\text{O}_{40})_2$ and AgCl@Ag. The high-resolution XPS spectrum in Figure 5b shows carbon peaks at 284, 286, and 288.6 eV. They can be ascribed to C1s electrons from C-C, N=C-N and π -excitation bonding in

($\text{CuC}_{10}\text{H}_{26}\text{N}_6$)₃($\text{PW}_{12}\text{O}_{40}$)₂, respectively.²⁴⁻²⁶ In the N1s spectrum (Figure 5c), a peak of 400.33 eV is attributed to N1s. The Ag3d peak in Figure 5d can be fitted with four components locating at 365.71, 366.12, 371.71, and 372.49 eV. The 366.12 and 372.49 eV components arise from the Ag^0 , whereas the 365.71 and 371.71 eV ones from the Ag^+ .²⁷ The XPS results confirm the coexistence of Ag^0 and AgCl in CPA-2. Figure 5e depicts a spectrum of Cl 2p. Two peaks were found at 197.75 eV and 199.25 eV, corresponding to $\text{Cl}2\text{p}_{3/2}$ and $\text{Cl}2\text{p}_{1/2}$, respectively. In Figure 5f, the peak at 935.00 eV can be assigned to 2p electrons from Cu^{2+} . The XPS results agree well with these results of XRD, elements mapping, TEM, and EDS mapping. Based on these characterizations, the Z-scheme ($\text{CuC}_{10}\text{H}_{26}\text{N}_6$)₃($\text{PW}_{12}\text{O}_{40}$)₂/AgCl@Ag compounds have been prepared successfully.

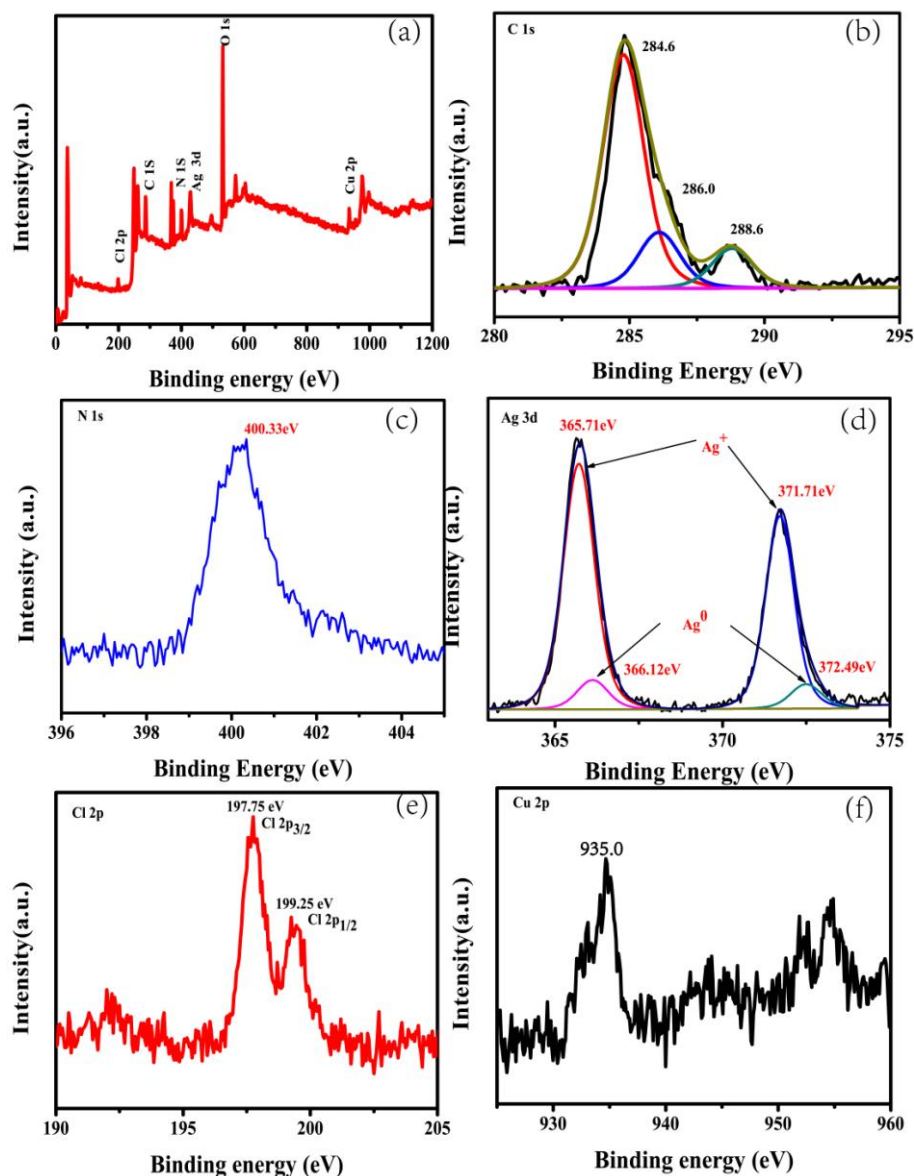


Figure 5. XPS spectra of CPA-2 sample: (a) survey spectrum, (b) C 1s, (c) N 1s, (d)

Ag 3d, (e) Cl 2p and (f) Cu 2p.

The porosity of the as-prepared samples is studied via N_2 adsorption/desorption isotherms (Figure S2) and BET results are shown in Table S1. CPA-0 has a BET surface area of $10.45 \text{ m}^2/\text{g}$. After loading the AgCl@Ag, the BET surface area increases slightly, tops at $17.86 \text{ m}^2/\text{g}$ for CPA-2, and then decreases. Larger surface

area can provide more active sites for photocatalytic reactions.²⁸ Compared with the CPA-0 (see Table. S1), the higher specific surface areas of CPA-1, CPA-2, CPA-3 and CPA-4 may get relatively higher photocatalytic activity.²⁹

The UV-vis absorption spectra of as-prepared photocatalysts are plotted in Figure 6. CPA-0 shows light absorption at the visible region thanks to the MCC modification. The adsorption edge was determined to 442 nm. After introduction of the AgCl@Ag, the composites exhibit remarkable enhancements of visible light absorption, which can be mainly attributed to the surface plasmon resonance (SPR) of Ag NPs.³⁰ Based on the Kubelka–Munk theory the bandgap energy (E_g) was calculated to 2.8eV for CPA-0.³¹

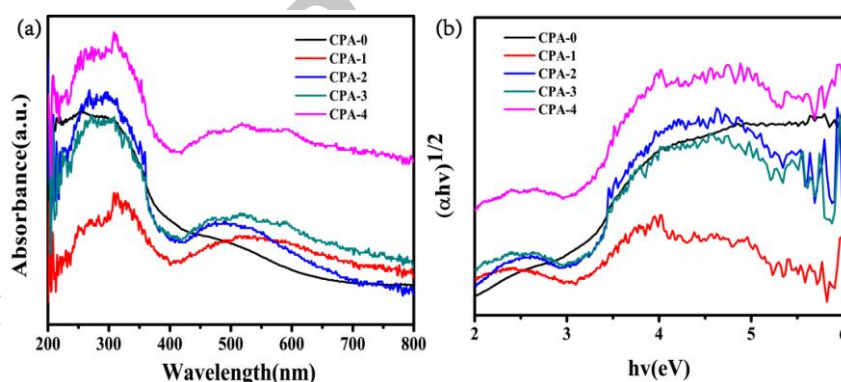


Figure 6. (a) UV–vis DRS of samples. (b) Plot of transformed KM function vs $h\nu$ for the corresponding samples.

The synthetic heterojunctions are capable to decontaminate stable and solid pollutant in aqueous ambience. The photodegradation of DNP and TC were evaluated with the existence of the as-prepared photocatalysts. Before the irradiation, the

photocatalysts were added in the DNP and TC solutions and stirred in the dark for 30 min to reach the adsorption-desorption equilibrium (Figure S3). The blank experiment in Figure 7 shows the concentration of DNP and TC remains unchanged without catalyst under light irradiation, indicating the high stability of DNP and TC.

As shown in Figure 7a, about 7% of DNP was adsorbed by CPA-2 prior to the photodegradation. On the contrary, CPA-1, CPA-3 and CPA-4 showed slightly higher adsorption for DNP, which should be ascribed to their different adsorption capacities. The pure CPA-0 can only degrade ~10% DNP under simulated sunlight. The rather low efficiency is attributed to the rapid recombination of photoinduced electrons-holes on a single semiconductor part. The photocatalytic efficiencies are significantly improved after AgCl@Ag introduction. The CPA-2 exhibited the highest photocatalytic activity for degrading the DNP (~65.0 % in 2 h). CPA-1, CPA-3 and CPA-4 own lower degradation efficiencies of ~ 54.5%, 57.5% and 57.1%, respectively. The removal efficiencies of DNP decreased in the order of CPA-2 (65.0%) > CPA-3(57.5%) > CPA-4 (57.1%) > CPA-1 (54.5 %) > CPA (0.11%). This clearly shows the suitable load of AgCl@Ag enhanced the photocatalytic ability of pure CPA-0. To understand the degradation dynamics, the degradation kinetics was shown in Figure 7b by using Langmuir–Hinshelwood model to fit the experimental data. The reaction rate constant of CPA-2 was highest in all samples, in line with its highest photocatalytic performance.

In addition to DNP, the degradation of TC under simulated sunlight was also investigated in details. As depicted Figure 7c, unlike the case of DNP, CPA showed better adsorption performance (~40%). This is attributed the pore size of CPAs is larger than the TC diameter. Interestingly, CPA-2 also owns the best performance in photocatalytic degradation of TC, resulting in the photocatalytic degradation efficiencies of 85% after 2h light irradiation. The TC removal rate increases with the Ag load from 0 to 9.75 wt%, but decreases with higher load percentages. This can be ascribed to the reduction of active sites after excessive metal loads,²⁸ which was well consistent with the results of BET. Similar to the DNP degradation trend, the pseudo-first-order reaction kinetics equation of TC degradation shows the CPA-2 has highest rate constant (Figure 7d). It is worth noting that the degradation abilities of CPA on TC were higher than DNP. The mainly reason is that TC is more easily adsorbed on the surface of photocatalyst where most photocatalytic reaction sites reside. Consequentially, the removal efficiencies are enhanced. The photocatalytic abilities of the CPA composites were also evaluated via degradations of model dyes of RhB and Cr (VI) ions. The excellent photocatalytic performances have been observed and depicted in Figure S4.

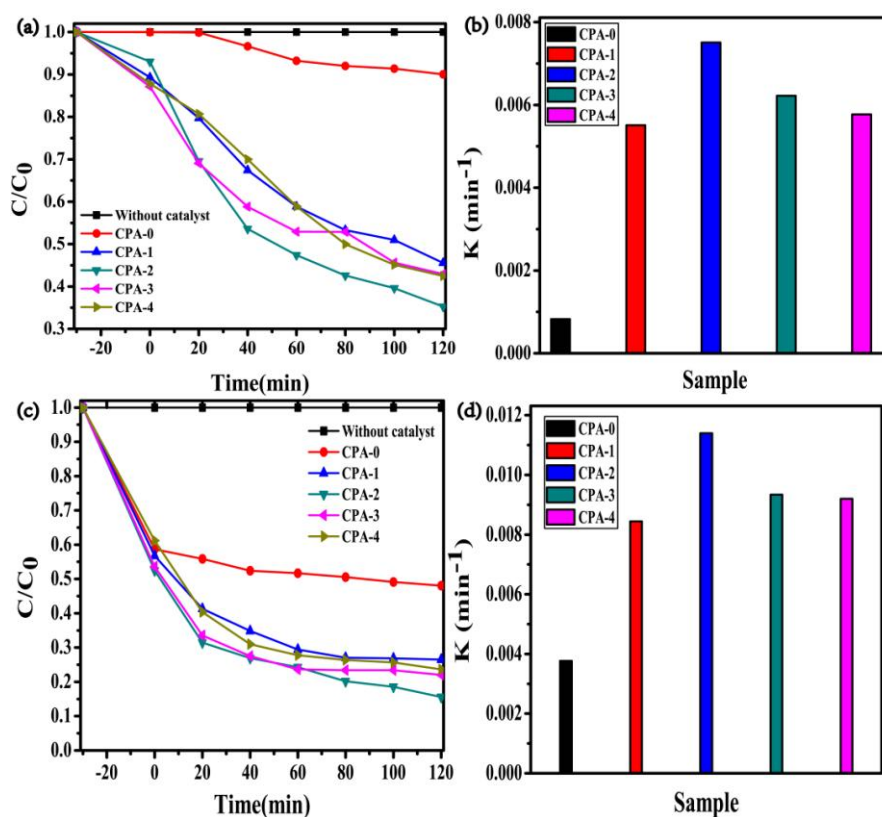


Figure 7. Photocatalytic performance of as-prepared photocatalysts. (a)

Photocatalytic degradation of DNP; (b) Comparison of the reaction rate constants of DNP. (c) Photocatalytic degradation of TC; (d) Comparison of the reaction rate constants of TC.

The PHE abilities of the samples are investigated. The PHE results of $(\text{CuC}_{10}\text{H}_{26}\text{N}_6)_3(\text{PW}_{12}\text{O}_{40})_2/\text{AgCl}@\text{Ag}$ were depicted in Figure 8a. As expected, CPA without $\text{AgCl}@\text{Ag}$ load does not serve H_2 production. This is attributed to the easy recombination of photogenerated electrons and holes on a single semiconductor. On the contrary, the $\text{AgCl}@\text{Ag}$ load will substantially increase the hydrogen production. With the increase of the load, the hydrogen production reaches an optimal value at the 9.75 wt% (CPA-2 $\sim 19.28 \mu\text{mol g}^{-1}\text{h}^{-1}$), then decreases. The cyclic stability of the

CPA-2 was also investigated. As viewed in Figure 8b, a stable hydrogen production rate of $19.28 \mu\text{mol g}^{-1}\text{h}^{-1}$ was kept in a 24-hour test. The composite was not decomposed or dissolved according to the XRD determination on the CPA-2 after PHE measurements (Figure S6). Thus, the synthesized CPA is stable. Hydrogen production results indicate the Z-scheme $(\text{CuC}_{10}\text{H}_{26}\text{N}_6)_3(\text{PW}_{12}\text{O}_{40})_2/\text{AgCl}@Ag$ composites have been designed successfully.

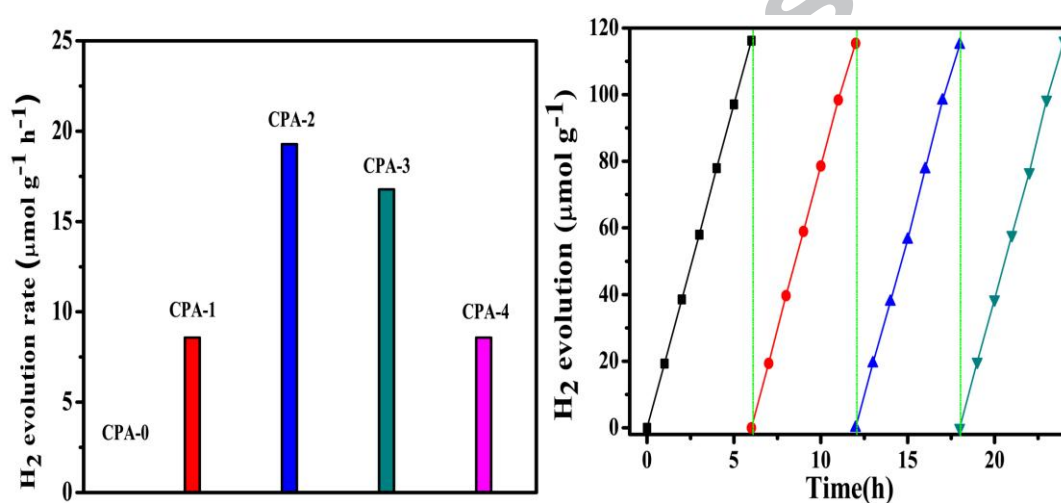


Figure 8. (a) The photocatalytic hydrogen evolution rate of samples. (b) The stability of CPA-2 under Simulated sunlight irradiation.

The photocatalysis depends on the photogenerated electron-hole separation and charge transfers.³² To evaluate the charge transfers and recombinations, the photoluminescence measurements were carried out.³³ As shown in Figure 9a, the PL peak of CPA-0 is higher than these of CPA-1, CPA-2, CPA-3 and CPA-4, indicating more probable electron-hole pair recombination via optical transitions on the unloaded matrix. Additionally, when the $\text{AgCl}@Ag$ was increased from 0% to 9.75%,

the PL emission peak of CPA-1, CPA-2 gradually decreases, corresponding to inhibited recombination of the photogenerated charge carriers.³⁴ Further increase amount of AgCl@Ag contents lead to slight loss of PL intensities as a result of less luminescent matrix of $(\text{CuC}_{10}\text{H}_{26}\text{N}_6)_3(\text{PW}_{12}\text{O}_{40})_2$.

The electrochemical impedance spectroscopy (EIS) was employed to evaluate the charge separations in the form of transient photocurrent. As shown in Figure 9b, the smaller arc radius indicates a lower charge transfer resistance.³⁵ The charge transfer resistance was in a sequence of CPA-2 < CPA-3 < CPA-4 < CPA-1 < CPA-0, suggesting charge transfer efficiency in the order of CPA-2 > CPA-3 > CPA-4 > CPA-1 > CPA-0. The transient photocurrent measurements were shown in Figure 9c. Similar trend was found in the order of CPA-2 > CPA-3 > CPA-4 > CPA-1 > CPA-0. The electrochemical test proves the enhanced charge separation abilities subjected to AgCl@Ag load, and is in line with the photocatalytic results. The bandgap of the matrix semiconductor is also studied. As shown in Figure 9d, the CPA-0 flat-band positions can be regulated by Mott-Schottky equation.^{36,7} Hence, the measurement of CPA-0's CB level was ca. -0.52 V (vs NHE) and the calculation of its VB level was ca. 2.28 V (vs NHE). On the other part, the E_{CB} and E_{VB} of AgCl are about -0.06 eV and 3.2 eV, respectively.³⁷

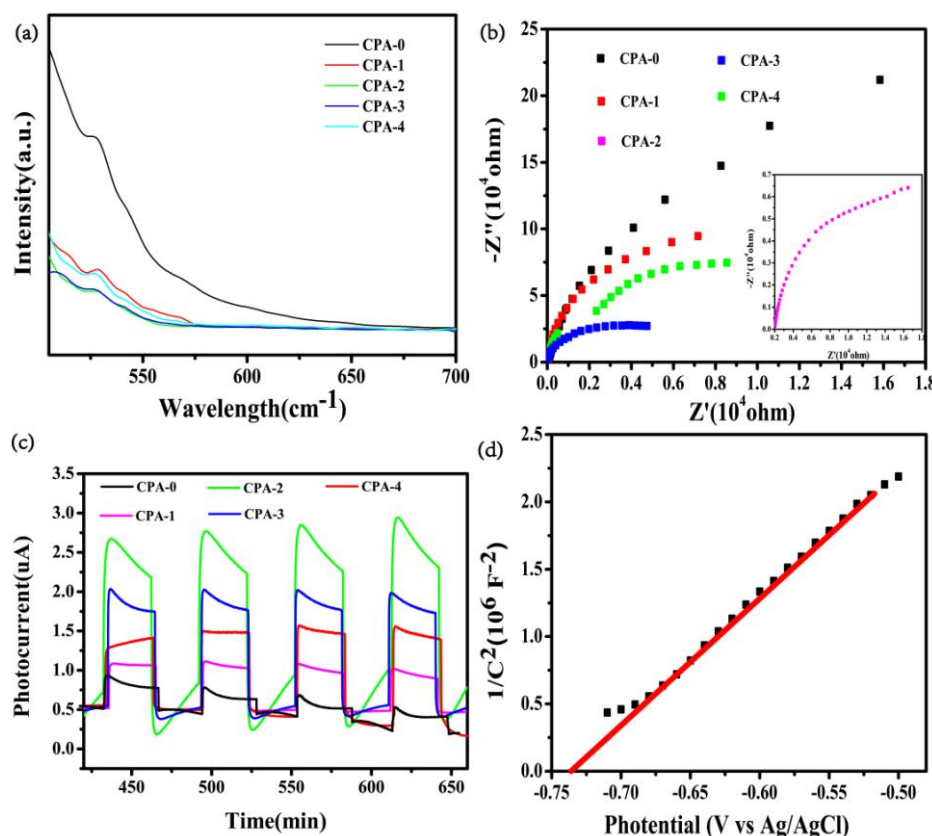


Figure 9. (a) PL spectra of samples; (b) EIS Nyquist plots of samples. (c) Transient photocurrent response of samples. (d) The Mott–Schottky plots of CPA-0.

The electron spin resonance spectroscopy is employed to identify the radicals during photocatalysis. As shown in Figure 10, strong characteristic peaks of DMPO- $\bullet\text{O}_2^-$ and DMPO- $\bullet\text{OH}$ were observed under simulated sunlight irradiation while the weak signal was detected in dark. Here, ESR results confirm that $\bullet\text{O}_2^-$ radicals and $\bullet\text{OH}$ radicals were mainly active species during the photodegradation process. This result is very consistent with Figure 11a. This further proves that the Z-scheme photocatalysts have been prepared successfully⁸.

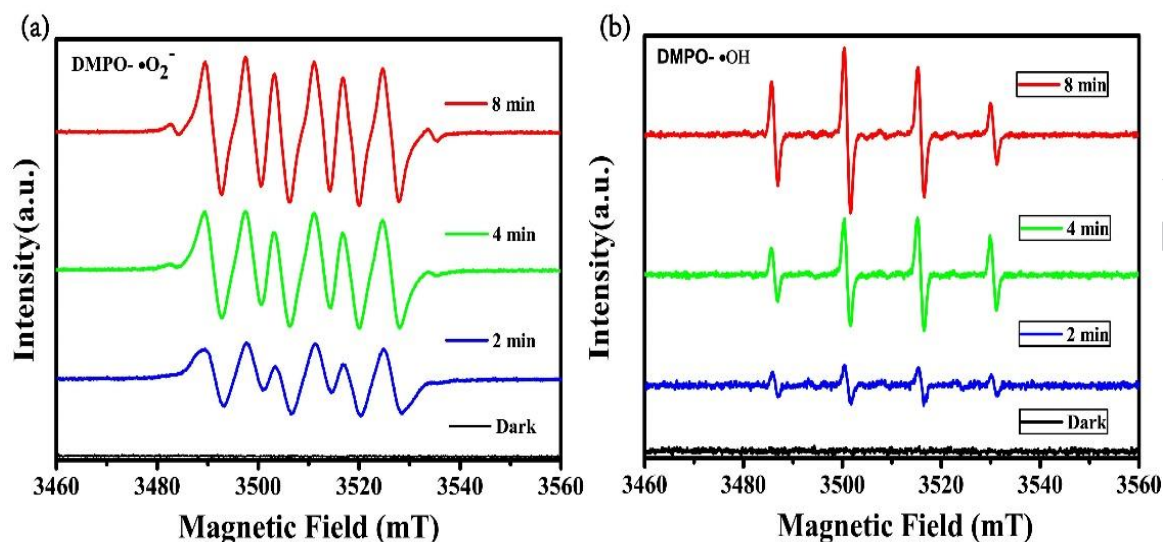


Figure 10. ESR spectra of CPA-2 in aqueous solution before and after light irradiation: (a) $\text{DMPO}-\cdot\text{O}_2^-$ and (b) $\text{DMPO}-\cdot\text{OH}$.

Based on the above experimental evidences, the photocatalytic mechanism of $(\text{CuC}_{10}\text{H}_{26}\text{N}_6)_3(\text{PW}_{12}\text{O}_{40})_2/\text{AgCl}@\text{Ag}$ is proposed. The $\cdot\text{O}_2^-$ and $\cdot\text{OH}$ were identified as the active radicals according to the ESR results. The $\cdot\text{O}_2^-$ radicals are hardly formed on the heterojunction because the E_{CB} of AgCl cannot reduce the residual O_2 in water to yield $\cdot\text{O}_2^-$, neither reduce H_2O to H_2 . Thus, the photogenerated electrons (e^-) in the CB of AgCl can transfer to the VB levels of CuPW. Meanwhile, the CuPW's VB levels are not positive enough so that it does not have sufficient oxidation ability to drive the oxidation process. The reduction forming H_2O to $\cdot\text{OH}$ has to happen on AgCl with higher VB levels. The difference of $\cdot\text{OH}/\text{H}_2\text{O}$ potential (ca. +2.27 V) suggests that photogenerated holes (h^+) in the VB of CuPW are combined with the electrons of AgCl. Moreover, the photogenerated electrons in the CB of CuPW reduces the adsorbed O_2 to yield $\cdot\text{O}_2^-$ or transfer $\text{H}_2\text{O}/\text{H}^+$ to H_2 . Both

$\cdot\text{O}_2^-$ and H^+ are powerful oxidative species to degrade pollutants. Furthermore, Ag NPs also can be excited to form electrons and holes, which can migrate to the CB of AgCl and the VB of CuPW via the Ag buffer. This increases the lifetime of the remaining holes (located at VB of AgCl) and electrons (resided at CB of $(\text{CuC}_{10}\text{H}_{26}\text{N}_6)_3(\text{PW}_{12}\text{O}_{40})_2$).⁶ The photocatalytic mechanism is then proposed and depicted in Figure 11. In a word, the Z-scheme retains strong oxidative and reductive abilities for efficient photocatalytic degradation of pollutants and hydrogen evolution.

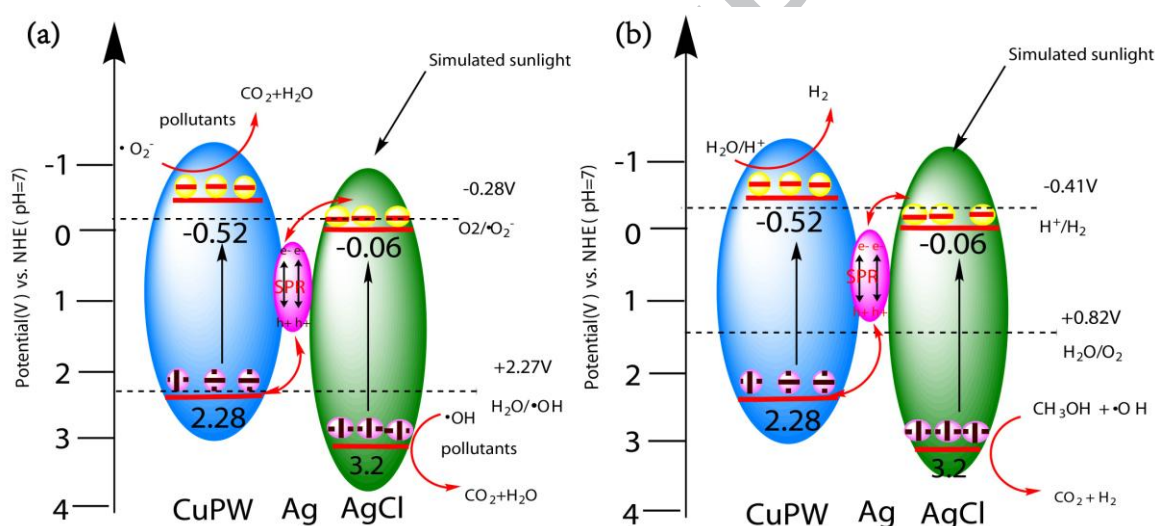


Figure 11. The mechanism the Z-scheme photocatalyst. (a) The degradation of pollutant, (b) the hydrogen evolution.

4. Conclusion

In conclusion, we successfully designed and realized the Z-scheme $(\text{CuC}_{10}\text{H}_{26}\text{N}_6)_3(\text{PW}_{12}\text{O}_{40})_2/\text{AgCl}@\text{Ag}$ photocatalysts via a simple hydrothermal-chemical co-deposition method. The macrocyclic coordination compound $(\text{CuC}_{12}\text{H}_{30}\text{N}_6)^{2+}$ was introduced into $\text{H}_3\text{PW}_{12}\text{O}_{40}$ to modify the

semiconductor band for visible light absorption and prevent water dissolution of the POM. The Z-scheme photocatalysts were formed via loading the AgCl@Ag onto the $(\text{CuC}_{10}\text{H}_{26}\text{N}_6)_3(\text{PW}_{12}\text{O}_{40})_2$ matrix. As a result, strong redox abilities were reached in the heterojunctions after delaying recombinations of the photogenerated charge carriers. The as-obtained $(\text{CuC}_{10}\text{H}_{26}\text{N}_6)_3(\text{PW}_{12}\text{O}_{40})_2/\text{AgCl@Ag}$ composites exhibit remarkable photocatalytic activities in pollutant degradations and hydrogen production. High rates of 65% and $19.28 \mu\text{mol g}^{-1} \text{h}^{-1}$ have been reached for solid DNP removal and hydrogen production under simulated sunlight radiation. Through experimental characterizations, the high photocatalytic performance of the AgCl@Ag joint with MCC-POM is attributed to effective separations of charge carriers between the heterojunctional peers, and deliberated designs to overcome reagents' shortcomings. Due to these advances, this work is hoped to debut a novel materials design roadmap in Z-scheme photocatalysts for practical applications of persistent pollutant removals and eco-fuel productions.

Acknowledgements

The authors acknowledge with thanks the financial support of the National Natural Science Foundation of China (21601149), Hunan 2011 Collaborative Innovation Centre of Chemical Engineering & Technology with Environmental Benignity and Effective Resource Utilization, profile funding of the Academy of Finland (No. 311934), European Regional Development Funding and the Oulu Council.

References

- [1] H. Li, Y. Zhou, W. Tu, J. Ye and Z. Zou, State - of - the - Art Progress in Diverse Heterostructured Photocatalysts toward Promoting Photocatalytic Performance. *dv. Funct. Mater.* 25 (2015) 998-1013. <https://doi.org/10.1002/adfm.201401636>.
- [2] F. Wu, X. Li, W. Liu and S. Zhang. Highly enhanced photocatalytic degradation of methylene blue over the indirect all-solid-state Z-scheme g-C₃N₄-RGO-TiO₂ nanoheterojunctions. *Appl. Surf. Sci.* 405 (2017) 60-70. <https://doi.org/10.1016/j.apsusc.2017.01.285>.
- [3] A.Y. Meng, B.C. Zhu, B. Zhong, L.Y. Zhang and B. Cheng. Direct Z-scheme TiO₂/CdS hierarchical photocatalyst for enhanced photocatalytic H₂-production activity. *Appl. Surf. Sci.* 422 (2017) 518-527. <https://doi.org/10.1016/j.apsusc.2017.06.028>.
- [4] P. Zhou, J. Yu and M. Jaroniec. All-solid-state Z-scheme photocatalytic systems. *Adv. Mater.* 26 (2014) 4920-4935. <https://doi.org/10.1002/adma.201400288>
- [5] Z. Song and Y.Q. He. Novel AgCl/Ag/AgFeO₂ Z-scheme heterostructure photocatalyst with enhanced photocatalytic and stability under visible light. *Appl. Surf. Sci.* 420 (2017) 911-918. <https://doi.org/10.1016/j.apsusc.2017.05.212>
- [6] B.T. Shi, H.Y. Yin, J.Y. Gong and Q.L. Nie. Ag/AgCl decorated Bi₄Ti₃O₁₂ nanosheet with highly exposed (001) facets for enhanced photocatalytic degradation of Rhodamine B, Carbamazepine and Tetracycline. *Appl. Surf. Sci.* 419 (2017) 614-623. <https://doi.org/10.1016/j.apsusc.2017.05.103>.

- [7] S. Sakthivel and H. Kisch, Daylight photocatalysis by carbon-modified titanium dioxide. *Angew. Chem. Int. Ed.* 42 (2003) 4908-4911. <http://doi.org/10.1002/anie.200351577>.
- [8] Z. Jiang, J. Pan, B. Wang and C.R. Li. Two dimensional Z-scheme AgCl/Ag/CaTiO₃ nano-heterojunctions for photocatalytic hydrogen production enhancement. *Appl. Surf. Sci.* 436 (2018) 519-526. <https://doi.org/10.1016/j.apsusc.2017.12.065>
- [9] C. Lydon, M.M. Sabi, M.D. Symes, D.L. Long, M. Murrie, S. Yoshii, H. Nojiri and L.Cronin. Directed assembly of nanoscale Co (ii)-substituted {Co₉[P₂W₁₅]₃} and {Co₁₄[P₂W₁₅]₄} polyoxometalates. *Chem. Commun.* 48 (2012) 9819-9821. <https://doi.org/10.1039/C2CC34865A>.
- [10] J.W. Zhang, Z.H. Liu, Y.C. Huang, J. Zhang, J. Hao and Y.G. Wei. Unprecedented X isomers of single-side triol-functionalized Anderson polyoxometalates and their proton-controlled isomer transformation. *Chem. Commun.* 51 (2015) 9097-9100. <https://doi.org/10.1039/c5cc02947c>.
- [11] A. Bayaguud, J. Zhang, R.N.N. Khan, J. Hao and Y.G. Wei. A redox active triad nanorod constructed from covalently interlinked organo-hexametalates. *Chem. Commun.* 50 (2014) 13150-13152. <https://doi.org/10.1039/c4cc06297c>.
- [12] Y. Hou, M. Nyman and M.A. Rodriguez. Soluble heteropolyniobates from the bottom of group IA. *Angew. Chem. Int. Ed.* 50 (2011) 12514-12517. <https://doi.org/10.1002/anie.201106642>.
- [13] T.M. Anderson, M.A. Rodriguez, F. Bonhomme, J.N. Bixler, T.M. Alam and M.Nyman. An aqueous route to [Ta₆O₁₉]₈⁻ and solid-state studies of isostructural niobium and tantalum oxide complexes. *Dalton Trans.* 40 (2007) 4517-4522. <https://doi.org/10.1039/B707636C>.

- [14] A. Troupis, A. Hiskia and E. Papaconstantinou. Synthesis of metal nanoparticles by using polyoxometalates as photocatalysts and stabilizers. *Angew. Chem Int. Ed.* 41 (2002) 1911-1914. <https://doi.org/10.1002/chin.200231245>.
- [15] A. Hiskia, A. Mylonas and E. Papaconstantinou. Comparison of the photoredox properties of polyoxometallates and semiconducting particles. *Chem. Soc. Rev.* 30 (2001) 62-69. <https://doi.org/10.1039/A905675K>.
- [16] E. Papaconstantinou. Photochemistry of polyoxometallates of molybdenum and tungsten and/or vanadium. *Chem. Soc. Rev.* 18 (1989) 1-31. <https://doi.org/10.1002/chin.198942344>.
- [17] A. Ioannidis and E. Papaconstantinou. Photocatalytic generation of hydrogen by 1: 12 heteropolytungstates with concomitant oxidation of organic compounds. *Inorg. Chem.* 24 (1985) 439-441. <https://doi.org/10.1002/chin.198525034>.
- [18] M.T. Pope and G.M. Varga Jr. Heteropoly blues. I. Reduction stoichiometries and reduction potentials of some 12-tungstates. *Inorg Chem.* 5 (1966) 1249-1254. <https://doi.org/10.1021/ic50041a038>.
- [19] H. Hori and K. Koike. New application of glycerin from a photochemical approach: dihydrogen formation from aqueous glycerin by use of giant polyoxometalate photocatalysts. *Energy & Fuels.* 19 (2005) 2209-2213. <https://doi.org/10.1021/ef050157i>.
- [20] T. Yamase and R. Watanabe. Photoredox chemistry of kegglin dodecatungstoborate $[BW_{12}O_{40}]_5^-$ and role of heterogeneous catalysis in hydrogen formation. *J. Chem. Soc. Dalton. Trans.* (1986) 1669-1675. <https://doi.org/10.1039/dt9860001669>.

- [21] Z. M. Zhang, T. Zhang, C. Wang, Z.K. Lin, L.S. Long and W.B. Lin. Photosensitizing metal–organic framework enabling visible-light-driven proton reduction by a Wells–Dawson-type polyoxometalate. *J. Am. Chem. Soc.* 137 (2015) 3197-3200. <https://doi.org/10.1021/jacs.5b00075>.
- [22] Y. Sun. Silver nanowires–unique templates for functional nanostructures. *Nanoscale*. 2 (2010) 1626-1642. <https://doi.org/10.1039/C0NR00258E>
- [23] X. Shi, Posysaev S, Huttula M, et al. Metal-Semiconductor Contacts: Metallic Contact between MoS₂ and Ni via Au Nanoglue. *Small*. 22 (2018) 1704526. <https://doi.org/10.1002/sml.201704526>
- [24] P. Qiu, H. Chen and F. Jiang. Cobalt modified mesoporous graphitic carbon nitride with enhanced visible-light photocatalytic activity. *RSC Adv.* 4 (2014) 39969-39977. <https://doi.org/10.1039/c4ra06451h>
- [25] J. Tian, L. Zhang, X. Fan, Y. Zhou, M. Wang, R. Cheng, M. Li, X. Kan, X. Jin, Z. Liu, Y. Gao and J. Shi. A post-grafting strategy to modify g-C₃N₄ with aromatic heterocycles for enhanced photocatalytic activity. *J. Mater. Chem. A*. 4 (2016) 13814-13821. <https://doi.org/10.1039/C6TA04297J>
- [26] Y. Wang, X. Wang and M. Antonietti, Polymeric graphitic carbon nitride as a heterogeneous organocatalyst: from photochemistry to multipurpose catalysis to sustainable chemistry. *Angew. Chem. Int. Ed.* 51 (2012) 68-89. <https://doi.org/10.1002/anie.201101182>.

- [27] C. Liang, C.G. Niu, X.J. Wen, S.F. Yang, M.C. Shen and G.M. Zeng. Effective removal of colourless pollutants and organic dyes by Ag@ AgCl nanoparticle-modified CaSn(OH)₆ composite under visible light irradiation. *New J. Chem.* 41 (2017) 5334-5346. <https://doi.org/10.1039/C7NJ00162B>.
- [28] S. Zhang, J. Li, X. Wang, Y. Huang, M. Zeng and J. Xu. In Situ Ion Exchange Synthesis of Strongly Coupled AgCl@Ag/g-C₃N₄ Porous Nanosheets as Plasmonic Photocatalyst for Highly Efficient Visible-Light Photocatalysis. *ACS Appl. Mater. Interf.* 6 (2014) 22116-22125. <https://doi.org/10.1021/am505528c>.
- [29] M. Aslam, M.T. Qamar, M.T. Soomro, I.M.I. Ismail, N. Salah, T. Almeelbi, M.A. Gondal and A. Hameed. The effect of sunlight induced surface defects on the photocatalytic activity of nanosized CeO₂ for the degradation of phenol and its derivatives. *Appl. Catal. B.* 180 (2016) 391-402. <https://doi.org/10.1016/j.apcatb.2015.06.050>
- [30] Y. Wang, Y. Zheng, C.Z. Huang and Y. Xia. Synthesis of Ag nanocubes 18–32 nm in edge length: the effects of polyol on reduction kinetics, size control, and reproducibility. *J. Am. Chem. Soc.* 135 (2013) 1941-1951. <https://doi.org/10.1021/ja311503q>
- [31] M. Butle. Photoelectrolysis and physical properties of the semiconducting electrode WO₂. *J. Appl. Phys.* 48 (1997) 1914-1920. <https://doi.org/10.1063/1.323948>
- [32] J. Zhang, G. Zhang, X. Chen, S. Lin, L. Mohlmann, G. Dolega, G. Lipner, M. Antonietti, S. Blechert and X. Wang. Co-monomer control of carbon nitride semiconductors to optimize hydrogen evolution with visible light. *Angew. Chem. Int. Ed. Engl.* 51 (2012) 3183–3187. <https://doi.org/10.1002/ange.201106656>

- [33] Q. Liang, Z. Li, Z.-H. Huang, F. Kang and Q.H. Yang. Holey graphitic carbon nitride nanosheets with carbon vacancies for highly improved photocatalytic hydrogen production. *Adv. Funct. Mater.* 25 (2015) 6885–6892. <https://doi.org/10.1002/adfm.201503221>.
- [34] G. Liu, G. Zhao, W. Zhou, Y. Liu, H. Pang, H. Zhang, D. Hao, X. Meng, P. Li, T. Kako and J. Ye. In situ bond modulation of graphitic carbon nitride to construct p–n homojunctions for enhanced photocatalytic hydrogen production. *Adv. Funct. Mater.* 26 (2016) 6822–6829. <https://doi.org/10.1002/adfm.201602779>.
- [35] H.B. Fang, N. Li, Z. Xue, Y. Zhang, Y.Z. Zheng and X. Tao. Efficient charge separation promoting visible-light-driven photocatalytic activity of MnO_x decorated WS₂ hybrid nanosheets. *Electrochem. Commun.* 72 (2016) 118–121. <https://doi.org/10.1016/j.elecom.2016.09.020>.
- [36] K. Gelderman, L. Lee, S.W. Donne. Flat-band potential of a semiconductor: using the Mott–Schottky equation. *J. Chem. Edu.* 84 (2007) 685. <https://doi.org/10.1021/ed084p685>.
- [37] L. Ye, J. Liu, C. Gong, L. Tian, T. Peng and L. Zan. Two different roles of metallic Ag on Ag/AgX/BiOX (X= Cl, Br) visible light photocatalysts: surface plasmon resonance and Z-scheme bridge. *ACS Catal.* 2 (2012) 1677–1683. <https://doi.org/10.1021/cs300213m>.

Figure and table captions

Figure 1. The XRD spectra of the $(\text{CuC}_{10}\text{H}_{26}\text{N}_6)_3(\text{PW}_{12}\text{O}_{40})_2$ loaded with different ratio of AgCl@Ag.

Figure 2. FTIR spectra of $(\text{CuC}_{10}\text{H}_{26}\text{N}_6)_3(\text{PW}_{12}\text{O}_{40})_2$ loaded with different ratio of AgCl@Ag.

Figure 3. The SEM of the as-prepared samples with different ratio, (a) CPA-0, (b) CPA-1, (c) CPA-2, (d) CPA-3, (e) CPA-4 and (f) CPA-2.

Figure 4. (a-c) TEM image of CPA-2, (d) HETEM image of CPA-2, (e) Dark field TEM images of CPA-2, (f) TEM-EDS mapping of CPA-2.

Figure 5. XPS spectra of CPA-2 sample: (a) survey spectrum, (b) C 1s, (c) N 1s, (d) Ag 3d, (e) Cl 2p and (f) Cu 2p.

Figure 6. (a) UV-vis DRS of samples. (b) Plot of transformed KM function vs $h\nu$ for the corresponding samples.

Figure 7. Photocatalytic performance of as-prepared photocatalysts. (a) Photocatalytic degradation of DNP; (b) Comparison of the reaction rate constants of DNP. (c) Photocatalytic degradation of TC; (d) Comparison of the reaction rate constants of TC.

Figure 8. (a) The photocatalytic hydrogen evolution rate of samples. (b) The stability of CPA-2 under Simulated sunlightlight irradiation.

Figure 9. (a) PL spectra of samples; (b) EIS Nyquist plots of samples. (c) Transient photocurrent response of samples. (d) The Mott–Schottky plots of CPA-0.

Figure 10. ESR spectra of CPA-2 in aqueous solution before and after light irradiation: (a) $\text{DMPO}\cdot\cdot\text{O}_2^-$ and (b) $\text{DMPO}\cdot\cdot\text{OH}$.

Figure 11. The mechanism the Z-scheme photocatalyst. (a) The degradation of pollutant, (b) the hydrogen evolution.

Graphical abstract

